

# Localized creation of yellow single photon emitting carbon complexes in hexagonal boron nitride

Anand Kumar,<sup>1,\*</sup> Chanaprom Cholsuk,<sup>1</sup> Ashkan Zand,<sup>1</sup> Mohammad Nasimuzzaman Mishuk,<sup>1</sup> Tjorben Matthes,<sup>1</sup> Falk Eilenberger,<sup>1,2,3</sup> Sujin Suwanna,<sup>4</sup> and Tobias Vogl<sup>1,2,†</sup>

<sup>1</sup>*Abbe Center of Photonics, Institute of Applied Physics,  
Friedrich Schiller University Jena, 07745 Jena, Germany*

<sup>2</sup>*Fraunhofer Institute for Applied Optics and Precision Engineering, 07745 Jena, Germany*

<sup>3</sup>*Max Planck School of Photonics, 07745 Jena, Germany*

<sup>4</sup>*Optical and Quantum Physics Laboratory, Department of Physics,  
Faculty of Science, Mahidol University, Bangkok 10400, Thailand*

(Dated: August 30, 2022)

Single photon emitters in solid-state crystals have received a lot of attention as building blocks for numerous quantum technology applications. Fluorescent defects in hexagonal boron nitride (hBN) stand out due to their high luminosity and robust operation at room temperature. The identical emitter fabrication at pre-defined sites is still challenging, which hampers the integration of these defects in optical systems and electro-optical devices. Here, we demonstrate the localized fabrication of hBN emitter arrays by electron beam irradiation using a standard scanning electron microscope with deep sub-micron lateral precision. The emitters are created with a high yield and a reproducible spectrum peaking at 575 nm. Our measurements of optically detected magnetic resonance have not revealed any addressable spin states. Using density functional theory, we attribute the experimentally observed emission lines to carbon-related defects, which are activated by the electron beam. Our scalable approach provides a promising pathway for fabricating room temperature single photon emitters in integrated quantum devices.

Keywords: Scanning electron microscope, density functional theory, carbon-based defects, localized fabrication, optically detected magnetic resonance

## I. INTRODUCTION

Many quantum photonic technologies, such as optical quantum computing and quantum communication, require sources of true single photons [1–6]. The generation of ideal single photons on demand, however, still remains to be a technical challenge. Due to their in principle simple operation requirements and possibilities for integration, solid-state color centers are promising candidates for single photon sources as opposed to semiconductor quantum dots. While the latter can emit simultaneously pure and indistinguishable single photons [7], the need for cryogenic cooling below 4 K prevents using quantum dots in broad applications. Within the class of the solid-state single photon emitters (SPEs) [8], color centers hosted by two-dimensional (2D) materials have the advantage of featuring an in-plane dipole that emits out-of-plane (in case of intra-layer defects) [9–11]. This simplifies the extraction and collection of the generated single photons, together with the fact that in atomically thin materials the emitters are not surrounded by any high refractive index material and are thus not affected by total internal or Fresnel reflection.

Single photon emitters hosted by 2D crystals have been observed initially in semiconducting transition metal dichalcogenides (TMDs) [12–16] and in insulating hexagonal boron nitride (hBN) [17]. The wide bandgap of hBN

allows for the formation of deep defect-induced energy levels that are well-isolated from the band edges. This in turn leads to a high quantum efficiency at room temperature [18] and is one of the reasons for the high single photon luminosity. Also contributing to this is a short excited-state lifetime [19] and the aforementioned high extraction efficiency. Unlike the nitrogen vacancy center in diamond, hBN emitters often have a strong coupling into the zero-phonon line (ZPL) with only weak phonon coupling that leads to coherent emission [20].

The quantum emitters in hBN can be fabricated in a rich variety of ways: thermal activation of naturally occurring emitters [17], plasma and chemical etching [19, 21], nanoindentation with an atomic force microscope (AFM) [22], strain-activation through transfer [23] or growth on pillared substrates [24], laser or gamma-ray damage [25, 26], and irradiation with electrons or ions [27–31]. While the strain activation localizes the emitter by default, many of the other fabrication techniques cause the emitter to form at random locations. Radiation damage has the potential for localization as well, since a laser or a charged particle beam can be easily focused onto a spot. The diffraction limit of electrons and ions is dependent on the particle energy and is typically of order a few nm, which allows one to place emitters with an extremely high accuracy.

In order to build integrated quantum devices with a scalable fabrication process, this precise control over the emitter location is crucial. Moreover, depending on the application, also spectral control is important. Quantum emitters have been experimentally reported with emis-

\* anand.kumar@uni-jena.de

† tobias.vogl@uni-jena.de

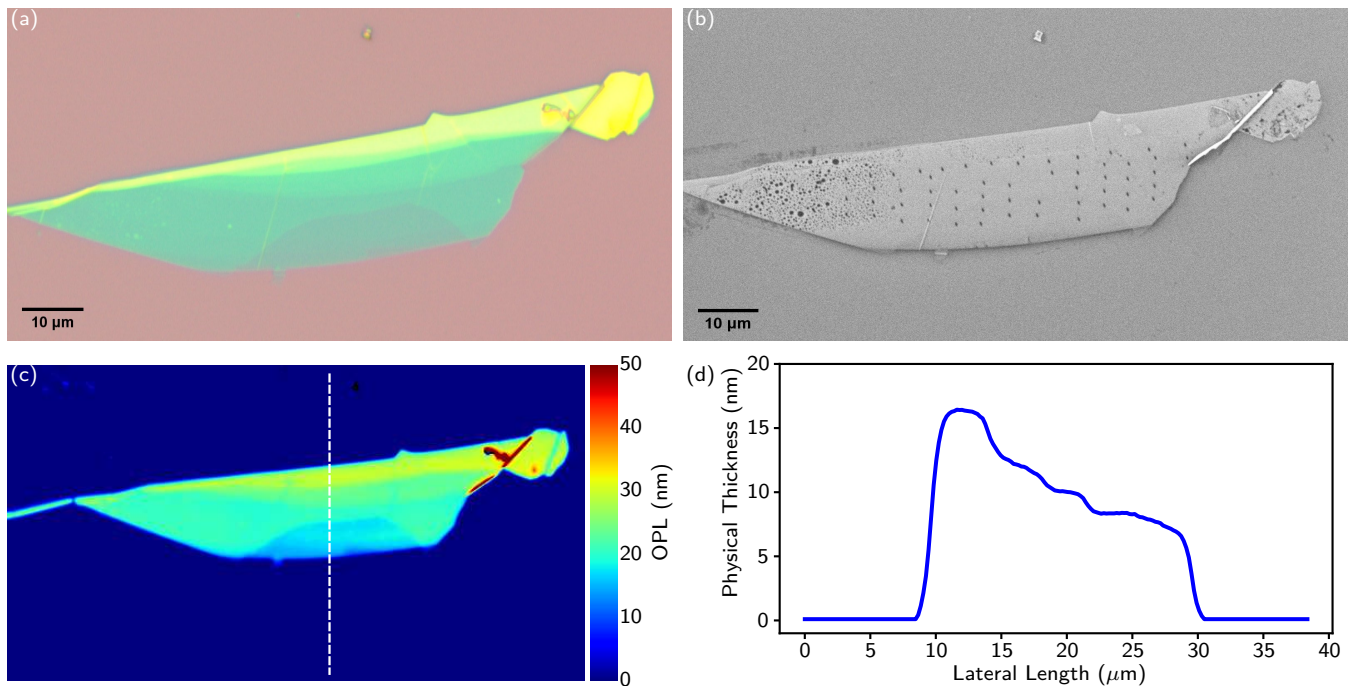


FIG. 1. (a) Optical microscope image of the exfoliated hBN flake on a Si/SiO<sub>2</sub> substrate. (b) SEM image of the flake after electron irradiation. The radiation sites are visible as distinctive dots. The image was created with a low electron dose to avoid the random creation of emitters. (c) Height map of the hBN flake with the color-bar depicting the optical path length (OPL) measured with a PSI. (d) Physical thickness of the flake calculated along the dashed line using RCWA simulations.

sion wavelengths in the UV [32], the entire visible spectrum [33], and in the NIR [34]. In addition, theoretical simulations have shown that hBN emitters cover important wavelengths for quantum technologies [35]. Spectral control is difficult to achieve because the nature and type of these defects is still a topic of ongoing research. Recent studies supported with density functional theory (DFT) calculations have identified carbon- and oxygen-related defects, as well as the negatively charged boron vacancy [36–39].

In this work, we address both issues of position and spectral control in the fabrication of quantum emitters in hBN. Using localized electron irradiation in a scanning electron microscope (SEM), we realize localized quantum emitters with a high yield. The high lateral resolution of the SEM allows us to restrict the emitter formation to sub-micron precision at pre-defined spots. While previous studies have found this to work reliably for blue emitters [28, 29], our method expands this to yellow emitters with a reproducible wavelength and without the need for high temperature annealing. We have also investigated the defects for addressable spin states through optically detected magnetic resonance (ODMR) [40–42]. Together with DFT calculations, we propose an atomic structure of the defect complex.

## II. EXPERIMENTAL SECTION

An hBN flake is mechanically exfoliated from a bulk crystal using a scotch tape onto a PDMS (polydimethylsiloxane) stamp. Thin flakes (typically in the range between 5 and 20 nm) are selected based on the optical contrast in a bright field microscope and transferred to a grid-patterned Si/SiO<sub>2</sub> substrate (see Methods). Figures 1(a) and (b) show an optical and SEM image, respectively, of a typical exfoliated hBN flake. The precise flake thickness is measured using a phase-shift interferometer (PSI), which measures the optical path length (OPL) through the flake and converts this using RCWA (rigorous coupled-wave analysis) simulations to the physical thickness. This technique was found to be highly accurate for 2D materials, yet is much faster than commonly used AFMs [9, 19]. An OPL map is shown in Figure 1(c), with the physical thickness along the dashed line shown in Figure 1(d).

The quantum emitters are created by irradiating the hBN flake with an electron beam from a scanning electron microscope without any pre-treatment. The high lateral resolution of the SEM allows us to restrict the interaction of the electrons with the hBN to small volumes, thereby localizing the emitter formation at any arbitrarily chosen spots with sub-micron precision. The number of emitters created depends on the fabrication parameters. For all experiments, we used an acceleration voltage of 3 kV and an electron current of 25 pA in the field-free

operation mode of the SEM. The theoretical resolution limit of our SEM is 2.8 nm, however, with the used beam alignment we estimate the beam diameter to be 256 nm. Since this is already the diffraction limit for the subsequent optical characterization, we did not optimize this any further. The dose is controlled by the irradiation time and we found optimal dwell times of 10 s which results in a particle fluence of  $7.7 \times 10^{17} \text{ cm}^{-2}$ . Pointing the electron beam to a single point produces single spots as is evident from the SEM image (see Figure 1(b)), however, higher doses allow us to directly write emitter ensembles and larger patterns (see Supplementary Section S1). We note that the fluence values used to record the SEM images ( $10^{13} \text{ cm}^{-2}$ ) are low compared to the conditions for emitter writing to avoid accidental fabrication of emitters.

It is known from the literature that many fabrication techniques require post-processing, in particular thermal annealing which either activates the emitter or at least enhances the intensity [29, 33, 43]. To investigate the impact of annealing on the emission properties (which are studied in detail in the next section), a flake is prepared with an emitter array of  $10 \times 4$  irradiated spots. Our photoluminescence (PL) images reveal that the emitter array that is present initially disappears after treatment with typical annealing conditions in a furnace at 850 °C under an inert argon atmosphere (600 mbar pressure) for 30 min (see Supplementary Section S2). We found that this annealing can activate other (uncorrelated) contaminants, but also heals ours through the SEM activated or created emitters. This suggests a high mobility and subsequent instability of the involved defects at such high temperatures. As a consequence, we conclude there is no post-processing necessary after the SEM treatment, which simplifies the fabrication. Other experiments on electron-irradiated hBN emitters confirm this [28, 31], however, Gale *et al.* reported that pre-annealing can enhance the emission [29] (which we have not observed).

The emitter fabrication with an electron beam is influenced by the electron beam diameter and electron scattering in the hBN lattice. To further study this interaction, an electron dose-dependent irradiation is performed by varying the electron irradiation time. An array of  $4 \times 3$  emitters is fabricated where each spot is irradiated for a different time. The photon count rate at each irradiated spot increases linearly with irradiation time. The optical characterization (for the details see the following section) and analysis are summarized in Supplementary Section S3. The linear increase can be attributed to the formation of increasingly large ensembles of emitters, suggesting a formation process governed by the Poisson statistics. Producing single emitters with a high yield thus requires careful calibration of the electron fluence.

### III. RESULTS AND DISCUSSION

#### A. Optical characterization

To identify if the fabrication parameters are feasible, we have optically characterized the created emitters with a commercial fluorescence lifetime imaging microscope (see Methods). All measurements have been performed at room temperature and with an excitation laser pulse repetition rate of 20 MHz. Our setup allows us to use different laser heads with fixed wavelengths of 375, 530, and 640 nm and pulse lengths in the range below 40 to 90 ps. The PL images for the different excitation energies are shown in Figures 2(a-c). As the crystal is always excited below the bandgap, there is only bright emission originating from the electron-irradiated spots. The brightness, however, strongly depends on the excitation energy. Note that the color scale for each PL map has been normalized such that the brightest emitter in Figure 2(a) under excitation with 375 nm laser light has a PL intensity of 1 a.u. As can be seen, the excitation is very inefficient in the UV and the emitters are the brightest under illumination with 530 nm laser light. We would like to mention that we have dynamically adapted the spacing between the irradiation spots such that our array has no a periodic spacing. This was due to the fact that the mechanically exfoliated flakes typically have random shapes and we did not want to fabricate emitters close to the crystal edges. The mean distance between irradiation spots is roughly 3  $\mu\text{m}$ . In the overlaid SEM and PL image (see Supplementary Section S4), it becomes clear that all irradiated spots have a corresponding bright spot in the PL image. The number of emitters per irradiated spot varies: while most of the time there is exactly one emitter present, sometimes there is a second emitter nearby (see Figure 2(d)) or emitter ensembles are created in the same spot (see Figure 2(e)). This is due to the Poisson statistics of the irradiation process.

The second-order correlation function  $g^{(2)}(\tau)$  of these emitters, however, reveals the presence of single photon emitters with the zero-delay peak under pulsed excitation dropping to 0.36 and 0.22 in Figure 2(f) and (g), respectively. A  $g^{(2)}(0)$  value below 0.5 proves a non-zero overlap with the single photon Fock state [44] and is the generally accepted criterion for single photon emitters. The details about the calculation of  $g^{(2)}(\tau)$  can be found in Supplementary Section S5. When spectrally-resolving the emission, a peak at 575 nm can be observed (see Figure 2(h)). It is worth noting that our long-pass filter has a cut-off wavelength of 550 nm to suppress the excitation laser at 530 nm which suppresses the detection of the emission partially. We therefore do not have access to the full spectral information about the emitter. In addition, the peak at 575 nm is near the Raman peak of hBN (the Raman shift of hBN at  $1360 \text{ cm}^{-1}$  [17] results in a peak at 571 nm). To determine if the 575 nm peak is the Raman peak we have also measured the temporally-resolved PL as shown in Figure 2(i). A fit

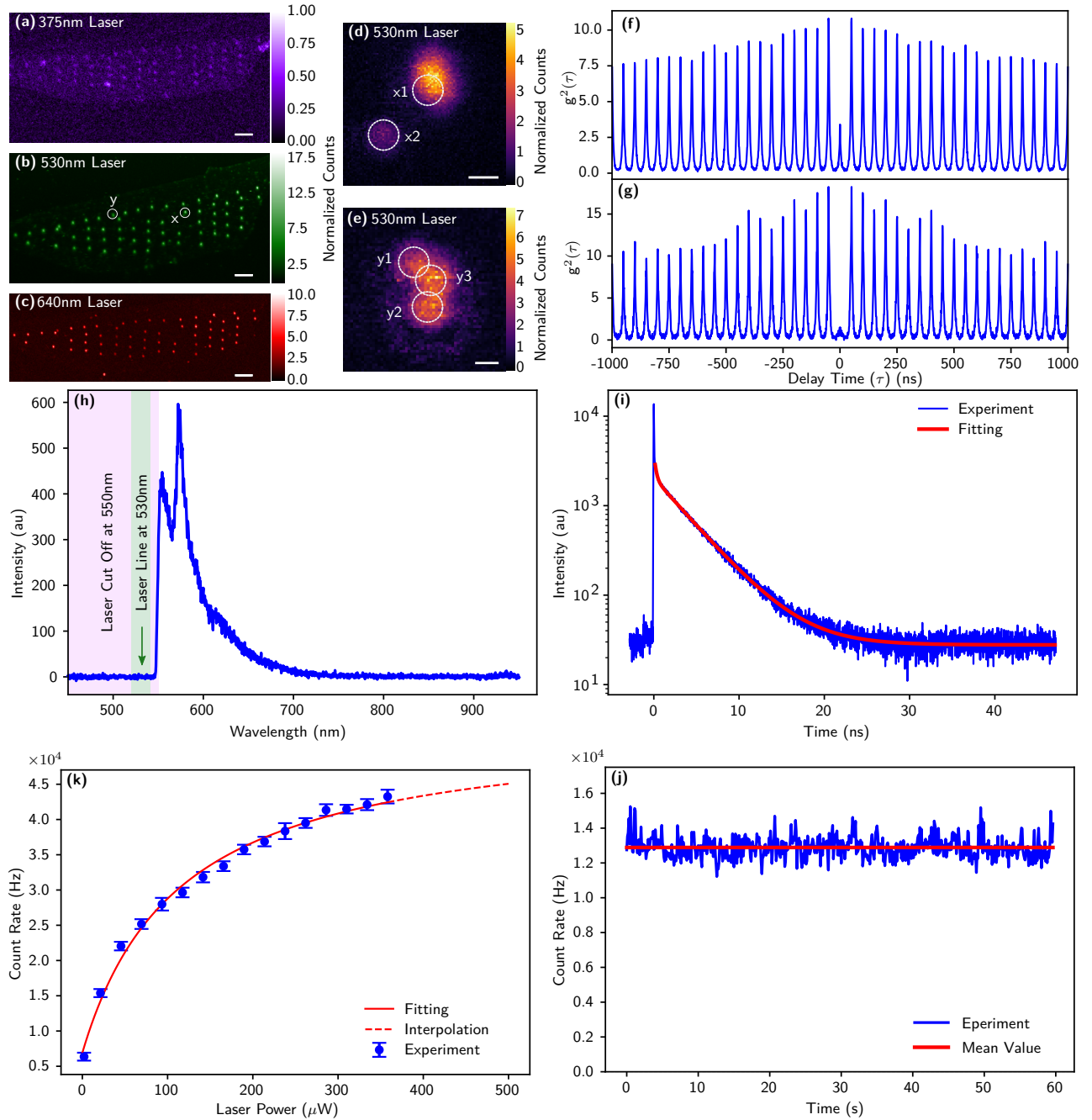


FIG. 2. Optical characterization of the emitter array using a time-resolved photoluminescence microscope. (a-c) PL maps of the array excited with a (a) 375 nm laser and a longpass filter at 405 nm, (b) 530 nm laser and a longpass filter at 550 nm, and (c) 640 nm and a bandpass filter transmitting from 650 to 720 nm. Each PL map is normalized to the maximum counts achieved with the 375 nm laser in (a). The white scale bar is  $5 \mu\text{m}$ . (d,e) PL maps of two individual irradiated spots excited at 530 nm marked with x and y in (b). The spots (x1,x2) and (y1,y2,y3) are individual SPEs with  $g^{(2)}(0) = (0.536, 0.224)$  at (x1, x2) and  $g^{(2)}(0) = (0.379, 0.363, 0.445)$  at (y1, y2, y3), respectively. The scale bar is  $0.5 \mu\text{m}$ . The second-order-correlation measurements of y1 and x2 are depicted in (f) and (g), respectively. (h) Spectrum of a sample SPE with a peak of the PL at 575 nm excited at 530 nm and detected with a longpass filter at 550 nm that cuts the emission partially. (i) The time-resolved PL measurement of the SPE reveals an excited-state lifetime of  $3.83(1)$  ns. The instrument response function was taken into account. (j) The power saturation curve of the emitter is similar to that of a two level system. The saturation intensity of 46.88 kHz and saturation power of  $114 \mu\text{W}$  is extracted from a fit. (k) The timetrace of a continuously excited emitter over 60 s demonstrates that the emitters exhibit no blinking or bleaching. The mean and standard deviation are  $12.9(6)$  kHz, implying a relative stability of 4.65%.

(taking into account the instrument response function) reveals an excited state lifetime of 3.83(1) ns, consistent with other reports of hBN quantum emitters [8, 19, 45]. The spectrally-resolved measurement of the lifetime and  $g^{(2)}(\tau)$  function have shown to be independent of the wavelength. We estimated that the 575 nm peak contributes too much to the spectrum to originate from Raman scattering (because this would change the photon statistics and emitter lifetime). Nevertheless, we do not assign this peak the ZPL, as this would require to have access to the complete emission spectrum.

The single photon intensity  $I$  as a function of the laser excitation power  $P$  reveals the typical saturation curve of a two-level system (see Figure 2(j)) and a fit with

$$I(P) = \frac{I_{\text{sat}}P}{P + P_{\text{sat}}} + I_{\text{d}} \quad (1)$$

allows us to extract a saturation power of  $P_{\text{sat}} = 114 \mu\text{W}$  and a maximum photon count rate of  $I_{\text{sat}} = 46.88 \text{ kHz}$ . The dark count rate  $I_{\text{d}}$  has a negligible effect on the fit due to the low dark count rate of our single photon detectors. The detected maximum photon count rate, however, is not the actual maximum emission rate because it is limited by the collection, transmission, and detection efficiencies. The former can be addressed by coupling the emitter with resonant cavities [45] that shape the emission to be more directional. Interestingly, we have not observed any blinking or bleaching of any of the emitters as shown by our time trace of an emitter in Figure 2(k). While this problem is known for many hBN emitters [46, 47], our irradiation seems to produce emitters that are not affected by this. We have also investigated the defects for addressable spin states through optically detected magnetic resonance [40–42]. Our preliminary measurements show no signature of ODMR as presented in Supplementary Section S6. This measurement is carried out on an ensemble of hBN emitters at room temperature. A comparative measurement with NV centers in diamond, however, demonstrated a significant ODMR contrast of that spin system and thereby verifying the general functionality of our ODMR setup.

## B. Statistical analysis

To understand if our process also produces high-quality emitters in general, we have analyzed the statistics over a larger data set containing 63 emitters fabricated on the same flake. We have decided to only include emitters hosted on the same flake in this analysis to remove the influence of the host crystal (e.g. through local strain) on the emitter properties. Figure 3(a) shows the distribution of the  $g^{(2)}(0)$  values, which reveals that most of the emitters can be classified as singles, while a few have  $g^{(2)}(0) > 1$  and are likely ensembles. The PL maps of a subset of these emitters are presented in Supplementary Section S7. The histogram of the lifetimes (see Figure

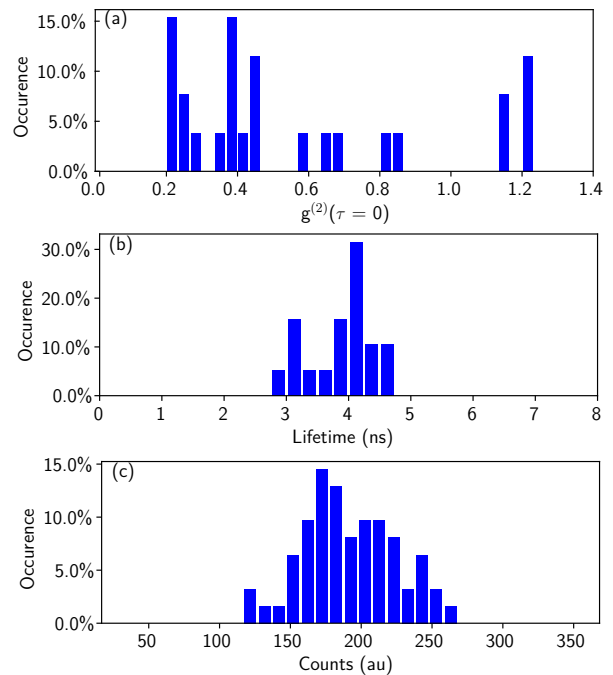


FIG. 3. Statistical distribution of photophysical properties from an emitter array on the same flake. (a) The distribution of second-order correlation function at zero time delay  $g^{(2)}(0)$  shows a majority of emitters have  $g^{(2)}(0) < 0.5$  and are therefore classified as single photon emitters. (b) Lifetime distribution of emitters with  $g^{(2)}(0) < 0.5$  extracted from the correlation function measurements. The mean value and standard deviation is 3.8(5) ns. (c) Brightness distribution of the emitter array excited with the 530 nm laser and a power of  $50 \mu\text{W}$ . The photon counts are obtained by integration over the spots in the PL map in Figure 2(b), each of which may contain a single emitter or ensembles thereof.

3(b)) reveals a mean lifetime of 3.8(5) ns (only counting emitters with  $g^{(2)}(0) \leq 0.5$ ). The consistency of the lifetime provides further evidence that the emitters produced are always the same without any additional decay channels for the excited state. We note that we extracted the lifetime for the histogram from the pulsed measurement of the second-order correlation function (see Supplementary Section S8). In the limit of zero excitation power, this method would yield the correct lifetime. In our case we used this method to reduce the measurement time, as we can measure lifetime and second-order correlation time simultaneously. The statistical distribution of the emitter brightness is presented in Figure 3(c), extracted from the PL map. For all 63 emitters presented in Figure 2(a), we wrote an automated algorithm that detects the emitter position and integrates over a diffraction-limited spot around its center (marked by the red boxes in Supplementary Section S9).

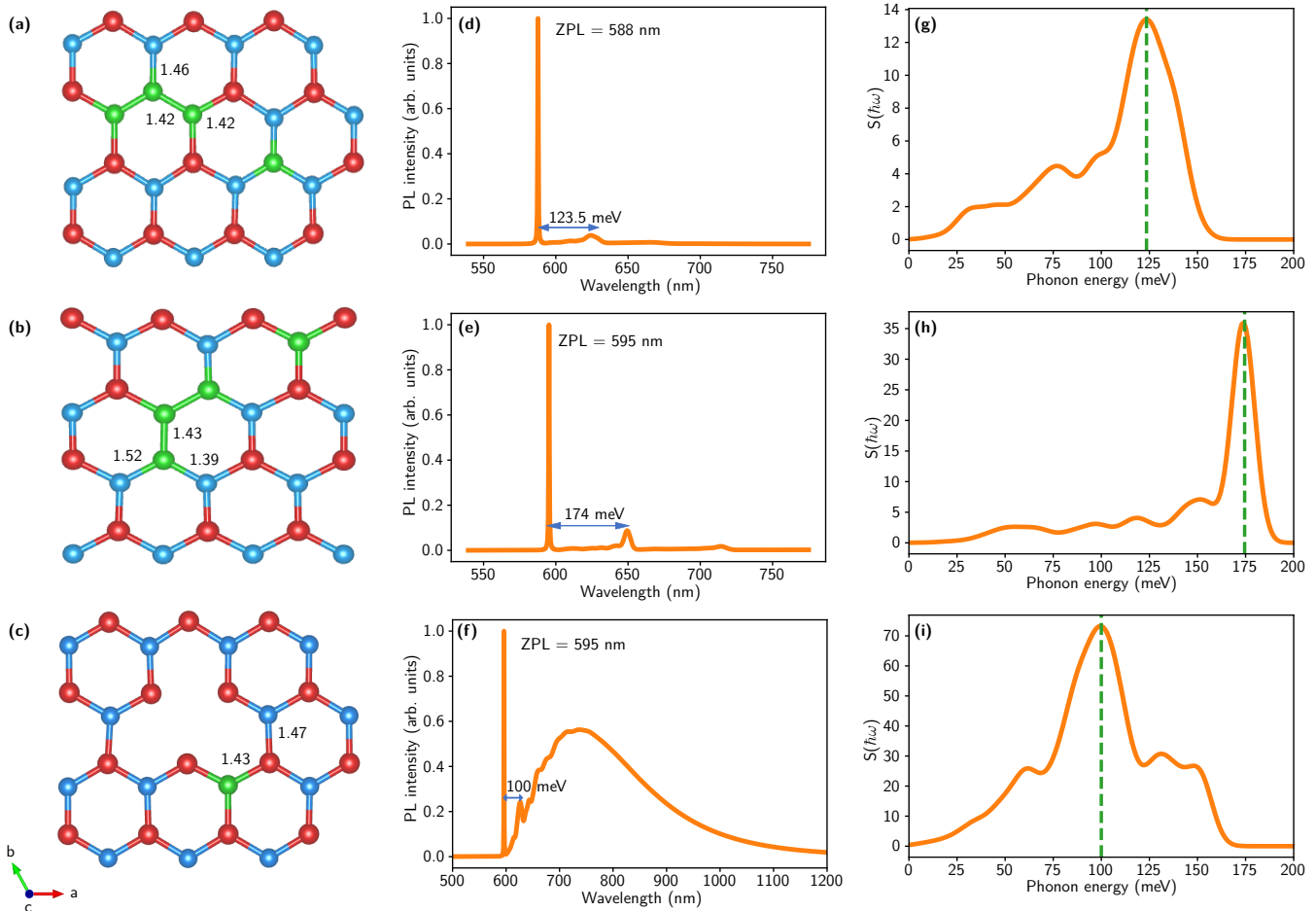


FIG. 4. Theoretical simulations. (a-c) Defect structures of potential candidates with the  $C_B C_N C_B C_N$  defect in two different configurations in (a) and (b), as well as the  $C_N V_N$  defect in (c). The boron atoms are blue, nitrogen red, and carbon green. The  $a$  and  $b$  directions are in-plane. (d-f) Theoretical photoluminescence spectra of the defect structures in (a-c), respectively, where the first peak belongs to ZPL while the second peak to the phonon sideband. The Huang-Rhys factor in (g-i) shows the corresponding contributions of the specific phonon modes to the PL spectra. The dashed line marks the peak of the phonon sideband. The broad PL emission in the near infrared in (f) is explained in the main text.

### C. Emitter identification with Density Functional Theory

To trace back the nature of the emitter, we carried out theoretical studies using density functional theory (see Methods). It is known that carbon contaminants are bonded to the surface during SEM imaging, which causes the typical dark frames. This suggests that carbon might be involved in the defect, as other calculations and experiments have demonstrated already [35, 36, 39]. Since the experimental spectra as shown in Figure 2(h) is a characteristic signature of all defects, we calculated the PL lineshape by employing the  $\Delta$ SCF method to determine the spectra of neutral and singly charged carbon complexes listed in Supplementary Section S10.

Our simulations identify the  $C_B C_N C_B C_N$  and  $C_N V_N$  complexes with the structural configurations depicted in Figure 4(a-c) as potential candidates for carbon-related

emitters with a transition energy (i.e. ZPL) in the yellow region. In addition to the ZPL, we also calculated the phonon sideband (PSB) to obtain the complete PL spectrum (see Figure 4(d-f)). The peaks can be identified by considering the spectral function of the electron-phonon coupling or Huang-Rhys (HR) factor as shown in Figure 4(g-i). The PSB peaks in the range of 100-175 meV, which is the typical range for hBN quantum emitters. Notably, the PL spectra of the  $C_N V_N$  defect exhibits a broad peak at 380 meV from the ZPL in the calculated PL spectrum. This phenomenon can be justified by the fact that these modes have a higher energy ( $> 200$  meV) than the zone-center longitudinal optical phonon mode ( $LO(\Gamma)$ ) [48]. As coupling to electrons scales with the inverse of the phonon wave vector from the Fröhlich interaction, the electron-phonon matrix element will subsequently diverge due to the singularity at this point and lead to broad PL. Based on the HR factor, the assignment

of the ZPL becomes evident. To identify the contributions to the ZPL, the HR factor yielded small values of 0.70, 0.97, and 4.40, corresponding to the configuration coordinates between ground and excited states shifted by  $0.376 \text{ amu}^{1/2}\text{\AA}$ ,  $0.368 \text{ amu}^{1/2}\text{\AA}$ , and  $0.953 \text{ amu}^{1/2}\text{\AA}$ , respectively, for the defect complexes shown in Figure 4(a-c). This reveals that the defects inherently emit at their assigned ZPL with only a weak contribution from phonon coupling in case of the  $C_B C_N C_B C_N$  configurations and with strong phonon coupling for the  $C_N V_N$  defect. This DFT calculation consequently proposes that  $C_B C_N C_B C_N$  is one of the potential candidates responsible for the emission, whereas  $C_N V_N$  is unlikely due to the mismatch of the PSB with the experiment. Moreover, the absence of any ODMR signature agrees with the most preferred spin-singlet configuration of  $C_B C_N C_B C_N$ .

We note that our DFT calculations did not consider temperature effects, which generally broaden the emission peaks and induce small shifts. Moreover, due to the finite computational resources, we have not been able to employ hybrid functionals (HSE06) to calculate the complete PL spectra, but rather used the PBE (Perdew, Burke, and Ernzerhof) functional in the generalized gradient approximation [49]. PBE is known to underestimate the bandgap and consequently also the energy difference between defect states [50–52]. We therefore expect the proposed defects to actually have slightly blue-shifted PL spectra that is then even closer to our experiment.

We finally answer the question of the formation mechanism. Electrons with an energy of 3 keV have not enough momentum for knock-on damage and to displace atoms. We also have not seen any diffusion of the defects. It is likely that the electrons can bond carbon to the hBN (which causes the black spots in the SEM image) and then break these bonds and re-organize them to form the carbon complexes. Another possibility is the change of the charge state of already present defects.

#### IV. CONCLUSIONS

We have demonstrated the localized fabrication of SPEs in exfoliated multilayers of hBN using focused electron beam irradiation with a well-defined set of emission properties and a high yield. Our process does not require any pre- or post-processing (e.g. thermal annealing) of the hBN crystals. All fabricated color centers emit consistently at 575 nm (2.16 eV). Our ODMR measurements have not revealed any addressable spin states. The theoretical analysis using DFT calculations allows us to propose possible atomic structures, namely of the carbon complex  $C_B C_N C_B C_N$ . The process is reproducible and repeatable and thus allows us to fabricate identical SPEs on demand and with deep sub-micron placement accuracy. Furthermore, our study also opens up a new way to understand the nature and photophysical properties of the defect-based emitters in hBN. As the method is

scalable and compatible with coupling to nanophotonics, we expect use in near-future quantum technology applications.

## METHODS

### Fabrication

Thin hBN flakes were prepared from bulk crystal (HQ Graphene) and mechanically-exfoliated using the scotch tape method to a visco-elastic polymer sheet (PDMS, Polydimethylsiloxane) available from Gel-Pak (WF-40-X4). Suitable thin flakes were then identified using a standard white-light microscope by optical contrast and transferred onto a silicon substrate with a 298 nm thick  $\text{SiO}_2$  capping layer by dry contact. To simplify the localization in the SEM, we have deposited markers on these substrates (before the hBN transfer) using an electron beam lithography (EBL) and metal lift-off process. This way we realized a cross grid pattern that allowed us to navigate to the desired flake easily.

### Electron Irradiation

The electron irradiated emitters is fabricated using a Helios NanoLab G3. The electron beam alignment is carried out at a different location on the substrate to avoid unintentional irradiation. To navigate on the sample and record images of the flakes, we used a low electron fluence of  $1.4 \times 10^{13} \text{ cm}^{-2}$  with a dwell time of 300 ns and 16 frame integration. To fabricate the emitters, each chosen spot is irradiated with dwell time of 10 s with fluence value of  $7.7 \times 10^{17} \text{ cm}^{-2}$  at a voltage of 3 kV and current of 25 pA.

### Optical characterization

The optical investigation of the quantum emitters is carried out using a commercial time-resolved confocal microscope (PicoQuant MicroTime 200). The setup offers three excitation laser with wavelengths 375, 530, and 640 nm with pulse lengths below ranging from 40 to 90 ps (depending on the wavelength). The excitation power for all measurements was around  $50 \mu\text{W}$  (unless stated otherwise). The detection path of the setup uses various notch filters (long- and bandpass) to block the excitation laser. The setup equipped with two SPADs (single photon avalanche diodes). The PL map of each flake is created using scanning the stage with 5 ms dwell time and a laser repetition rate of 20 MHz. The PL signal is collected using a  $100\times$  dry immersion objective with high numerical aperture (NA) of 0.9. The assembly of two SPADs in both arms of a 50:50 beamsplitter enables us to measure second-order correlation function. The data analysis of the correlation function as well as lifetime measurements

is performed with the built-in software (that also takes the instrument response function into account). The data acquisition times for these measurements was 1 min per emitter. The spectrometer (Andor Kymera 328i) is attached to one of the exit ports of the optical setup to collect the spectrum of the emitters.

### ODMR measurements

The ODMR measurements were carried out using a custom-built optical setup at room temperature. The optical setup consists of a continuous-wave diode laser with an excitation wavelength of 520 nm together with a white light source for imaging the sample. A 20 $\times$  magnification objective with an NA 0.4 is used to excite sample and confocally collect the fluorescence signal. The fluorescence signal is filtered with a longpass filter (cutoff wavelength 600 nm) and detected using a SPAD (ID Quantique ID100). A wire with a diameter of 100  $\mu$ m is used to apply a microwave field using a portable vector network analyzer up to 4 GHz (PocketVNA). The wire is attached to the XYZ translational mount align with excitation spot. To compare our results with an established spin system that exhibits the ODMR effect, we purchased fluorescent nanodiamonds with >500 NV centers per particle from Sigma-Aldrich Chemie GmbH in liquid solution. The solution is dropcasted over a standard Si/SiO<sub>2</sub> wafer with a 298 nm thermally-grown oxide layer. Afterwards, the sample is left to dry in ambient condition before characterization in the ODMR setup.

### DFT calculations

All spin-polarized calculations were performed using the Vienna Ab initio Simulation Package (VASP) with a plane wave basis set [53, 54] and the projector augmented wave (PAW) as the pseudopotentials [55, 56]. The generalized gradient approximation of Perdew, Burke, and Ernzerhof (PBE) formalism was employed [49]. A pristine hBN monolayer was created with a 15 Å vacuum layer and a 7  $\times$  7  $\times$  1 containing 98 atoms to minimize the layer-layer and neighboring-cell interactions, respectively. Point defects were then inserted at the center of the supercell and optimized with relaxation of only internal coordinates allowed. All geometry relaxations were performed with an energy cutoff at 500 eV and the to-

tal energy converged with the accuracy of 10<sup>-4</sup> eV. The Brillouin zone integration was sampled by a 3  $\times$  3  $\times$  1 reciprocal space grid. For the excited-state calculations, we used the  $\Delta$ SCF method, in which the electronic occupations are manually constrained (see also Supplementary Section S10). The PyPhotonics python package was used for post-processing the PL workflows [57] while the PHONOPY package [58] was utilized for phonon calculations of the 7  $\times$  7  $\times$  1 supercell size of the ground-state configuration, which was proven to be sufficiently large to capture the low-energy phonons.

### DATA AVAILABILITY

All data from this work is available from the authors upon reasonable request.

### NOTES

The authors declare no competing financial interest.

### ACKNOWLEDGMENTS

This work was funded by the Deutsche Forschungsgemeinschaft (DFG, German Research Foundation) - Projektnummer 445275953. The authors acknowledge support by the German Space Agency DLR with funds provided by the Federal Ministry for Economic Affairs and Climate Action BMWK under grant number 50WM2165 (QUICK3). T.V. and F.E. are funded by the Federal Ministry of Education and Research (BMBF) under grant number 13N16292 and 13XP5053A, respectively. The major instrumentation used in this work was funded by the Free State of Thuringia via the projects 2015 FOR 0005 (ACP-FIB) and 2017 IZN 0012 (InQuoSens). C.C. acknowledges a Development and Promotion of Science and Technology Talents Project (DPST) scholarship by the Royal Thai Government. The computational experiments were supported by resources of the Friedrich Schiller University Jena supported in part by DFG grants INST 275/334-1 FUGG and INST 275/363-1 FUGG. We thank Jeetendra Gour for the fabrication of the cross grid patterned substrate and acknowledge fruitful discussions with Igor Aharonovich on the potential assignment of the Raman peak.

---

[1] J. L. O'Brien, A. Furusawa, and J. Vučković, Photonic quantum technologies, *Nat. Photon.* **3**, 687 (2009).  
 [2] K. Mukai and N. Hatano, Discrete-time quantum walk on complex networks for community detection, *Phys. Rev. Res.* **2**, 023378 (2020).  
 [3] A. Aspuru-Guzik and P. Walther, Photonic quantum simulators, *Nat. Phys.* **8**, 285–291 (2012).

[4] J. Cai, A. Retzker, F. Jelezko, and M. B. Plenio, A large-scale quantum simulator on a diamond surface at room temperature, *Nat. Phys.* **9**, 168–173 (2013).  
 [5] A. I. Lvovsky, B. C. Sanders, and W. Tittel, Optical quantum memory, *Nat. Photon.* **3**, 706–714 (2009).  
 [6] H.-K. Lo, M. Curty, and K. Tamaki, Secure quantum key distribution, *Nat. Photon.* **8**, 595 (2014).



- [7] P. Senellart, G. Solomon, and A. White, High-performance semiconductor quantum-dot single-photon sources, *Nat. Nanotechnol.* **12**, 1026 (2017).
- [8] I. Aharonovich, D. Englund, and M. Toth, Solid-state single-photon emitters, *Nat. Photon.* **10**, 631–641 (2016).
- [9] T. Vogl, M. W. Doherty, B. C. Buchler, Y. Lu, and P. K. Lam, Atomic localization of quantum emitters in multilayer hexagonal boron nitride, *Nanoscale* **11**, 14362 (2019).
- [10] M. Hoese, P. Reddy, A. Dietrich, M. K. Koch, K. G. Fehler, M. W. Doherty, and A. Kubanek, Mechanical decoupling of quantum emitters in hexagonal boron nitride from low-energy phonon modes, *Sci. Adv.* **6**, eaba6038 (2020).
- [11] M. Hoese, M. K. Koch, F. Breuning, N. Lettner, K. G. Fehler, and A. Kubanek, Single photon randomness originating from the symmetric dipole emission pattern of quantum emitters, *Appl. Phys. Lett.* **120**, 044001 (2022).
- [12] J. Klein, M. Lorke, M. Florian, F. Sigger, L. Sigl, S. Rey, J. Wierzbowski, J. Cerne, K. Müller, E. Mitterreiter, and et al., Site-selectively generated photon emitters in monolayer MoS<sub>2</sub> via local helium ion irradiation, *Nat. Commun.* **10**, 2755 (2019).
- [13] J. Klein, L. Sigl, S. Gyger, K. Barthelmi, M. Florian, S. Rey, T. Taniguchi, K. Watanabe, F. Jahnke, C. Kastl, and et al., Engineering the luminescence and generation of individual defect emitters in atomically thin mos<sub>2</sub>, *ACS Photonics* **8**, 669–677 (2021).
- [14] A. Srivastava, M. Sidler, A. V. Allain, D. S. Lembke, A. Kis, and A. Imamoglu, Optically active quantum dots in monolayer wse<sub>2</sub>, *Nat. Nanotechnol.* **10**, 491–496 (2015).
- [15] Y.-M. He, G. Clark, J. R. Schaibley, Y. He, M.-C. Chen, Y.-J. Wei, X. Ding, Q. Zhang, W. Yao, X. Xu, and et al., Single quantum emitters in monolayer semiconductors, *Nat. Nanotechnol.* **10**, 497–502 (2015).
- [16] P. Tonndorf, R. Schmidt, R. Schneider, J. Kern, M. Buscema, G. A. Steele, A. Castellanos-Gomez, H. S. J. van der Zant, S. M. de Vasconcellos, and R. Bratschkitsch, Single-photon emission from localized excitons in an atomically thin semiconductor, *Optica* **2**, 347 (2015).
- [17] T. T. Tran, K. Bray, M. J. Ford, M. Toth, and I. Aharonovich, Quantum emission from hexagonal boron nitride monolayers, *Nat. Nanotechnol.* **11**, 37–41 (2016).
- [18] N. Nikolay, N. Mendelson, E. Özelci, B. Sontheimer, F. Böhm, G. Kewes, M. Toth, I. Aharonovich, and O. Benson, Direct measurement of quantum efficiency of single-photon emitters in hexagonal boron nitride, *Optica* **6**, 1084 (2019).
- [19] T. Vogl, G. Campbell, B. C. Buchler, Y. Lu, and P. K. Lam, Fabrication and deterministic transfer of high-quality quantum emitters in hexagonal boron nitride, *ACS Photonics* **5**, 2305–2312 (2018).
- [20] A. Kubanek, Coherent quantum emitters in hexagonal boron nitride, *Adv. Quantum Technol.* , 2200009 (2022).
- [21] N. Chejanovsky, M. Rezai, F. Paolucci, Y. Kim, T. Rendler, W. Rouabah, F. Fávoro de Oliveira, P. Herlinger, A. Denisenko, S. Yang, I. Gerhardt, A. Finkler, J. H. Smet, and J. Wrachtrup, Structural attributes and photodynamics of visible spectrum quantum emitters in hexagonal boron nitride, *Nano Lett.* **16**, 7037 (2016).
- [22] X. Xu, Z. O. Martin, D. Sychev, A. S. Lagutchev, Y. P. Chen, T. Taniguchi, K. Watanabe, V. M. ShalaeV, and A. Boltasseva, Creating quantum emitters in hexagonal boron nitride deterministically on chip-compatible substrates, *Nano Lett.* **21**, 8182–8189 (2021).
- [23] N. V. Proscia, Z. Shotan, H. Jayakumar, P. Reddy, C. Cohen, M. Dollar, A. Alkauskas, M. Doherty, C. A. Meriles, and V. M. Menon, Near-deterministic activation of room-temperature quantum emitters in hexagonal boron nitride, *Optica* **5**, 1128 (2018).
- [24] C. Li, N. Mendelson, R. Ritika, Y. Chen, Z.-Q. Xu, M. Toth, and I. Aharonovich, Scalable and deterministic fabrication of quantum emitter arrays from hexagonal boron nitride, *Nano Lett.* **21**, 3626 (2021), pMID: 33870699.
- [25] S. Hou, M. D. Birowosuto, S. Umar, M. A. Anicet, R. Y. Tay, P. Coquet, B. K. Tay, H. Wang, and E. H. T. Teo, Localized emission from laser-irradiated defects in 2d hexagonal boron nitride, *2D Mater.* **5**, 015010 (2017).
- [26] T. Vogl, K. Sripathy, A. Sharma, P. Reddy, J. Sullivan, J. R. Machacek, L. Zhang, F. Karouta, B. C. Buchler, M. W. Doherty, and et al., Radiation tolerance of two-dimensional material-based devices for space applications, *Nat. Commun.* **10**, 1202 (2019).
- [27] S. Choi, T. T. Tran, C. Elbadawi, C. Lobo, X. Wang, S. Juodkazis, G. Seniutinas, M. Toth, and I. Aharonovich, Engineering and localization of quantum emitters in large hexagonal boron nitride layers, *ACS Appl. Mater. Interfaces* **8**, 29642 (2016).
- [28] C. Fournier, A. Plaud, S. Roux, A. Pierret, M. Rosticher, K. Watanabe, T. Taniguchi, S. Buil, X. Quélin, J. Barjon, and et al., Position-controlled quantum emitters with reproducible emission wavelength in hexagonal boron nitride, *Nat. Commun.* **12**, 3779 (2021).
- [29] A. Gale, C. Li, Y. Chen, K. Watanabe, T. Taniguchi, I. Aharonovich, and M. Toth, Site-specific fabrication of blue quantum emitters in hexagonal boron nitride, *ACS Photonics* **9**, 2170–2177 (2022).
- [30] B. Shevitski, S. M. Gilbert, C. T. Chen, C. Kastl, E. S. Barnard, E. Wong, D. F. Ogletree, K. Watanabe, T. Taniguchi, A. Zettl, and S. Aloni, Blue-light-emitting color centers in high-quality hexagonal boron nitride, *Phys. Rev. B* **100**, 155419 (2019).
- [31] H. Ngoc My Duong, M. A. P. Nguyen, M. Kianinia, T. Ohshima, H. Abe, K. Watanabe, T. Taniguchi, J. H. Edgar, I. Aharonovich, M. Toth, and et al., Effects of high-energy electron irradiation on quantum emitters in hexagonal boron nitride, *ACS Appl. Mater. Interfaces* **10**, 24886–24891 (2018).
- [32] R. Bourrellier, S. Meuret, A. Tararan, O. Stéphan, M. Kociak, L. H. G. Tizei, and A. Zobelli, Bright uv single photon emission at point defects in h-BN, *Nano Lett.* **16**, 4317 (2016).
- [33] T. T. Tran, C. Elbadawi, D. Totonjian, C. J. Lobo, G. Grosso, H. Moon, D. R. Englund, M. J. Ford, I. Aharonovich, M. Toth, and et al., Robust multicolor single photon emission from point defects in hexagonal boron nitride, *ACS Nano* **10**, 7331–7338 (2016).
- [34] R. Camphausen, L. Marini, S. A. Tawfik, T. T. Tran, M. J. Ford, and S. Palomba, Observation of near-infrared sub-poissonian photon emission in hexagonal boron nitride at room temperature, *APL Photonics* **5**, 076103 (2020).
- [35] C. Cholsuk, S. Suwanna, and T. Vogl, Tailoring the emission wavelength of color centers in hexagonal boron nitride for quantum applications, *Nanomaterials* **12**, 2427

- (2022).
- [36] N. Mendelson, D. Chugh, J. R. Reimers, T. S. Cheng, A. Gottscholl, H. Long, C. J. Mellor, A. Zettl, V. Dyakonov, P. H. Beton, S. V. Novikov, C. Jagadish, H. H. Tan, M. J. Ford, M. Toth, C. Bradac, and I. Aharonovich, Identifying carbon as the source of visible single-photon emission from hexagonal boron nitride, *Nat. Mater.* **20**, 321 (2021).
- [37] M. Fischer, J. M. Caridad, A. Sajid, S. Ghaderzadeh, M. Ghorbani-Asl, L. Gammelgaard, P. Bøggild, K. S. Thygesen, A. V. Krashennnikov, S. Xiao, M. Wubs, and N. Stenger, Controlled generation of luminescent centers in hexagonal boron nitride by irradiation engineering, *Sci. Adv.* **7**, eabe7138 (2021).
- [38] V. Ivády, G. Barcza, G. Thiering, S. Li, H. Hamdi, J.-P. Chou, Ö. Legeza, and A. Gali, Ab initio theory of the negatively charged boron vacancy qubit in hexagonal boron nitride, *NPJ Comput. Mater.* **6**, 41 (2020).
- [39] P. Auburger and A. Gali, Towards ab initio identification of paramagnetic substitutional carbon defects in hexagonal boron nitride acting as quantum bits, *Phys. Rev. B* **104**, 075410 (2021).
- [40] A. Gottscholl, M. Diez, V. Soltamov, C. Kasper, D. Krauß, A. Sperlich, M. Kianinia, C. Bradac, I. Aharonovich, V. Dyakonov, and et al., Spin defects in hBN as promising temperature, pressure and magnetic field quantum sensors, *Nat. Commun.* **12**, 4480 (2021).
- [41] H. L. Stern, Q. Gu, J. Jarman, S. Eizagirre Barker, N. Mendelson, D. Chugh, S. Schott, H. H. Tan, H. Siringhaus, I. Aharonovich, and et al., Room-temperature optically detected magnetic resonance of single defects in hexagonal boron nitride, *Nat. Commun.* **13**, 618 (2022).
- [42] G.-Q. Liu, X. Feng, N. Wang, Q. Li, and R.-B. Liu, Coherent quantum control of nitrogen-vacancy center spins near 1000 Kelvin, *Nat. Commun.* **10**, 1344 (2019).
- [43] C. Li, Z.-Q. Xu, N. Mendelson, M. Kianinia, M. Toth, and I. Aharonovich, Purification of single-photon emission from hbn using post-processing treatments, *Nanophotonics* **8**, 2049 (2019).
- [44] P. Grünwald, Effective second-order correlation function and single-photon detection, *New J. Phys.* **21**, 093003 (2019).
- [45] T. Vogl, R. Lecamwasam, B. C. Buchler, Y. Lu, and P. K. Lam, Compact cavity-enhanced single-photon generation with hexagonal boron nitride, *ACS Photonics* **6**, 1955–1962 (2019).
- [46] M. K. Boll, I. P. Radko, A. Huck, and U. L. Andersen, Photophysics of quantum emitters in hexagonal boron-nitride nano-flakes, *Opt. Express* **28**, 7475 (2020).
- [47] H. L. Stern, R. Wang, Y. Fan, R. Mizuta, J. C. Stewart, L.-M. Needham, T. D. Roberts, R. Wai, N. S. Ginsberg, D. Klenerman, S. Hofmann, and S. F. Lee, Spectrally resolved photodynamics of individual emitters in large-area monolayers of hexagonal boron nitride, *ACS Nano* **13**, 4538 (2019).
- [48] T. Q. P. Vuong, G. Cassabois, P. Valvin, A. Ouerghi, Y. Chassagneux, C. Voisin, and B. Gil, Phonon-photon mapping in a color center in hexagonal boron nitride, *Phys. Rev. Lett.* **117**, 097402 (2016).
- [49] J. P. Perdew, K. Burke, and M. Ernzerhof, Generalized gradient approximation made simple, *Phys. Rev. Lett.* **77**, 3865 (1996).
- [50] J. R. Reimers, A. Sajid, R. Kobayashi, and M. J. Ford, Understanding and calibrating density-functional-theory calculations describing the energy and spectroscopy of defect sites in hexagonal boron nitride, *J. Chem. Theory Comput.* **14**, 1602 (2018).
- [51] S. A. Tawfik, S. Ali, M. Fronzi, M. Kianinia, T. T. Tran, C. Stampfl, I. Aharonovich, M. Toth, and M. J. Ford, First-principles investigation of quantum emission from hbn defects, *Nanoscale* **9**, 13575 (2017).
- [52] A. Alkauskas, B. B. Buckley, D. D. Awschalom, and C. G. V. D. Walle, First-principles theory of the luminescence lineshape for the triplet transition in diamond NV centres, *New J. Phys.* **16**, 073026 (2014).
- [53] G. Kresse and J. Furthmüller, Efficiency of ab-initio total energy calculations for metals and semiconductors using a plane-wave basis set, *Comput. Mater. Sci.* **6**, 15 (1996).
- [54] G. Kresse and J. Furthmüller, Efficient iterative schemes for ab initio total-energy calculations using a plane-wave basis set, *Phys. Rev. B* **54**, 11169 (1996).
- [55] P. E. Blöchl, Projector augmented-wave method, *Phys. Rev. B* **50**, 17953 (1994).
- [56] G. Kresse and D. Joubert, From ultrasoft pseudopotentials to the projector augmented-wave method, *Phys. Rev. B* **59**, 1758 (1999).
- [57] S. A. Tawfik and S. P. Russo, Pyphotronics: A python package for the evaluation of luminescence properties of defects, *Comput. Phys. Commun.* **273**, 108222 (2022).
- [58] A. Togo and I. Tanaka, First principles phonon calculations in materials science, *Scr. Mater.* **108**, 1 (2015).